Light-scattering experiments on phase-separation dynamics in binary fluid mixtures

Andrew Cumming
Department of Physics, University of Florida, Gainesville, Florida 32611

Pierre Wiltzius
AT&T Bell Laboratories, Murray Hill, New Jersey 07974

Frank S. Bates and Jeffrey H. Rosedale
Department of Chemical Engineering and Material Science, University of Minnesota, Minneapolis, Minnesota 55455
(Received 31 July 1991)

We present the method and results of two phase-separation experiments performed on the binary-polymer blend polyisoprene-poly(ethylene-propylene). Elastic light scattering and optical microscopy were used to follow the phase separation after quenches into the coexistence region of the phase diagram. For off-critical quenches, we observed the formation of spherical droplets which obtained nearly monodisperse radius distributions over some fraction of the free-growth period. These results are interpreted within the framework of a heterogeneous nucleation process and diffusion-driven dynamics. For critical quenches, we observed the well-known bicontinuous infinite-cluster morphology normally associated with spinodal decomposition, but with two distinct growth modes. In the bulk, we observed $L(t)\sim t^{1/3}$, which is consistent with diffusion-driven dynamics, whereas near the sample walls we obtained a fast growth with $L(t)\sim t^{3/2}$, inconsistent with either diffusion- or interface-driven dynamics. We attribute this large exponent to wetting effects, but still lack any theoretical understanding of the phonomenon.

PACS number(s): 05.70.Fh, 64.60.−i, 68.45.Gd, 61.14.Hg

I. INTRODUCTION

In recent years there has been a great deal of attention paid to systems which display nonequilibrium statistical mechanical behavior. There have been investigations of the kinetics and dynamics of phase transitions from both the theoretical and experimental points of view for some two decades or more now [1,2]. Two-component mixtures which show a miscibility gap comprise a particularly accessible class of such systems, wherein the phase transition under study is phase separation, either via spinodal decomposition or nucleation and growth, depending on the parameters used. Studies have been carried out in a broad diversity of systems, including micellar solutions [3], colloids [4], metal alloys [5], glasses [6], polymers [7,8], and critical binary fluids [9].

In order to study phase-separation kinetics, one must have a system in which phase separation can be initiated at a time of the investigators' choosing. This requires a firm knowledge of that system's phase diagram, in order that abrupt changes in one or more of the thermodynamic fields (usually temperature) can be effected to take the system from the region of the phase diagram where it does not separate into phases, i.e., where the homogeneous mixture is thermodynamically stable, to the region where it will separate.

We were motivated in the present research by a dearth of experimental results concerning the early stages of nucleation and growth and spinodal decomposition in previous work with binary fluid systems. In the case of the classical work by Knobler and co-workers [10] and Goldburg and co-workers [11], intermediate- and late-stage data could be collected only by staying very close to the coexistence curve ($t=|T-T_{\rm coex}|/T_{\rm coex}\leq 10^{-5}$). In the case of spinodal decomposition, these studies relied on critical slowing down to render the dynamics accessible. We have found relief from this constraint, as have others, [12,13] by studying polymer blends. We used mixtures of poly(ethylene-propylene) (PEP) at molecular weight (MW) equal to 5000, and polyisoprene (PI) at MW equal to 2000, which were very well suited to phase-separation studies because their interactions are of the appropriate strength to all on the critical temperature to be somewhere near room temperature. Furthermore, with viscosities of order 400 times that of water, the dynamics of phase separation were sufficiently slow to allow them to be followed, even at early and intermediate times, for reduced temperatures t of order 10^{-3} to 10^{-2}. The phase diagram for this system is depicted in Fig. 1.

The difference in the index of refraction between PEP and PI is just under 1% for the pure materials, and so ranges from essentially 0 to 0.2%, depending on quench depth, for the constituent phases in this separation process. Typical domain sizes ranged from 100 nm to 100 μm in these experiments, and so were best probed with elastically scattered light. We chose a charge-coupled-device (CCD) detector for our light-scattering experiments because of its two-dimensional nature, allowing us to perform azimuthal averages of the structure function in the case of isotropic scattering, or to detect anisotropies in the scattering signal, should they exist. In addition, these detectors have a superb dynamic range (14

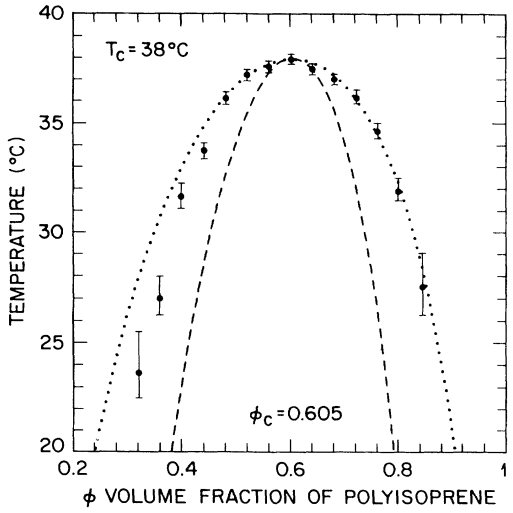

FIG. 1. Phase diagram for the polyisoprene-poly(ethylene-propylene) system used to study phase-separation dynamics of critical and off-critical quenches. The results communicated in this paper are for the samples at $\varphi_{PI}=0.48$ and 0.60, in the case of the monodisperse spheres and fast mode, respectively. The dashed and dotted curves are the spinodal and coexistence curves, respectively, for a best-fit Flory-Huggins free-energy-density calculation. The data are the experimentally measured phase-separation thresholds for various concentrations.

bits) and adequate sensitivity to detect even the slightest scattering signal with only 5 mW of incident laser power, in principle being capable of detecting single photons, and in practice capable of detecting as few as ten impinging on a single pixel. The practical ramification of this sensitivity is that "snapshots" of the structure function can be made with exposure times as low as 0.1 s. The speed is important when collecting data from time-evolving systems.

By exploiting the unique characteristics of our light-scattering apparatus, and indeed those of the PEP-PI system, we were able to observe and characterize several novel phenomena in the area of phase-separation kinetics. In off-critical quenches on the PEP-rich side of the phase diagram ($\phi=0.48$), we observed the nucleation of minority-phase droplets, which proceeded to grow as expected for free diffusion; i.e., the radius $R(t)\sim t^{1/2}$. The novelty lay in the fact that for a finite window of time the distribution of droplet radii narrowed to the point where the polydispersity decreased to below 3%, and then increased again. It was during the monodisperse regime that the droplets' radii grew like $t^{1/2}$. We sought to understand this phenomenon in terms of a heterogeneous nucleation process, in which there is some fixed number of sites on which minority-phase droplets can nucleate. Once they are saturated, no new droplets are introduced. The explanation of the observed dynamics depends on the assumption that the droplets are not interacting. At later times, however, they do begin to interact, and growth proceeds by the Lifshitz-Slyozov (LS) [14], process with no new nucleation, regardless of whether the initial nucleation was homogeneous or heterogeneous. Thus the observation of a monodisperse droplet distribution during some early time window is a hallmark of heterogeneous nucleation. This discriminant can be used whenever structure data can be collected at early enough times. In previous studies [15] of nucleation in low-molecular-weight simple liquid systems, reduced times that were sufficiently early were not accessible, and initial nucleation was almost universally attributed to the homogeneous process, more or less by default. This is an important consideration when, for instance, interpreting data in the context of the Langer-Schwartz [16] theory, which only applies to the case of homogeneous nucleation.

The second major result of the present research is the discovery of a fast growth mode in the case of critical quenches. It has been well established theoretically [17,36] and experimentally [18] in the nonlinear pattern-coarsening regime of spinodal decomposition that the pattern-length scale grows with time as $L(t)\sim t^{1/3}$ in the case that material transport is by diffusion alone, and $L(t)\sim t$ in the case that bulk hydrodynamic flows driven by surface tension are allowed. By contrast, we have observed power-law growth with an exponent $L(t)\sim t^{3/2}$, which, on the basis of a dynamical scaling argument, we have shown to arise from a two-dimensional scattering structure. We conjecture that this phenomenon is associated with some long-range van der Waals mediated, or wetting effect. Recently, the role played by wetting in binary systems has received much theoretical and experimental attention, [19–21] although a derivation for the $t^{3/2}$ behavior has eluded theorists.

The remainder of the paper will consist of sections on each of the following topics: The apparatus which was devised for making the elastic light-scattering measurements, preparation and characterization of the samples, detailed descriptions of each of the novel phenomena, and finally some concluding remarks.

II. EXPERIMENT: CCD LIGHT-SCATTERING APPARATUS

A cutaway view of the scheme for mounting and temperature controlling the sample is shown in Fig. 2(a). The assembly consisted of a brass block which contained passages through which temperature-regulated water was passed. A close-tolerance aluminum sample carrier was inserted into this brass block, with a thermally conducting paste enhancing thermal contact between these pieces. The sample cell was held in position by an aluminum plate with a hole in the center to allow the incident laser beam to pass through and was also brought into thermal contact with the carrier with the help of conducting paste. The water circuit in the brass block was fed from the circulation pump of a Lauda bath and circulator. The water in the bath was regulated at the quench temperature to an accuracy of ± 5 mK. This water supply was switched by a solenoid-actuated valve. The valve was open for the quench and the duration of the phase-separation experiment, but closed for the anneal period and at all other times, as shown in Fig. 2(b). During annealing, with the water flow turned off, the temperature

of the sample was regulated by a Lakeshore DRC82 temperature controller operating a Minco self-adhesive heater tape attached to the front of the brass block. A thermistor situated beside the sample cell itself provided the regulation temperature to the controller. The sample cell consisted of two fused quartz disks 21 mm in diameter and 1.2 mm in thickness. Annular spacers of outside diameter 16 mm, inside diameter 10 mm, and thicknesses between 0.2 and 1.0 mm were used to contain the polymer blend between the quartz disks. Some additional experiments were performed with wedged samples, wherein the thickness ranged from 0 to 1.0 mm over the 21 mm diameter of the disks. The entire assembly was then sealed with a bead of epoxy on the outside of the annular spacer, between the disks. In order to prevent oxidization the sample material was packaged in these sealed cells in a dry-argon-gas environment.

As noted earlier, the detector we chose to measure the structure factor for these phase-separating samples was a CCD chip. A Tektronix 512×512 pixel device with Peltier cooling regulated to −40 °C was used throughout the present experiments. The pixel size for this device is 27 μm×27μm. At a 50-kHz readout rate, this CCD was capable of 14-bit dynamic range, allowing single exposure determinations of the elastic structure factor for all accessible momentum transfers. This apparatus was packaged commercially by Photometrics Ltd. to include a controller unit which enabled data to be acquired automatically by a dedicated personal computer. The major effect of the basic design of the apparatus was expended on behalf of the problem of directing the scattered light from the sample's scattering volume onto the approximately 1 cm×1 cm CCD chip. We required all of the light scattered by up to 45° to be directed onto the chip, corresponding to photon momentum transfer magnitudes in the sample of up to 75 000 cm^{-1}. A further requirement of the design dictated that all rays emanating from the entire scattering volume in a given direction (corresponding to a given momentum transfer) be directed onto a single pixel of the CCD. This rather subtle design feature was indeed a challenge to satisfy, but was determined to be necessary to achieve the full resolution of the detector.

Figure 3 is a schematic representation of the light-scattering apparatus in plan view. The light from a 5-mW helium-neon (He-Ne) laser, linearly polarized perpendicular to the plane of the page, impinged on the sample cell. The scattered light was collected by an off-axis paraboloidal mirror, whose focus is essentially at the position of the scattering volume. In this configuration, the mirror served to columnate the scattered ray bundle, whereupon it could be passed through a pair of positive lenses which share a focus, and onto the CCD. The confocal pair of lenses, which acted as a beam reducer, were moved together along their optical axis to facilitate the focusing of light of a given momentum transfer onto a single pixel on the detector. Naturally, the CCD also had to be adjusted along the optical axis of the beam reducer

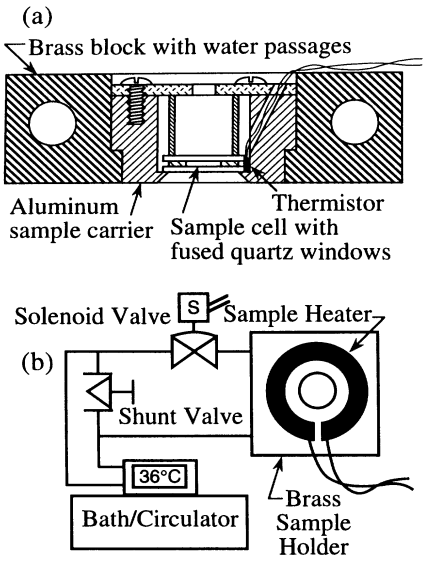

FIG. 2. Apparatus for holding the sample and effecting rapid changes in its temperature. (a) A cutaway view of the brass block which held the sample carrier and sample cell in these experiments. Water of a controlled temperature was passed through the holes, maintaining a constant temperature in the cell during phase separation. A thermistor gauged the sample temperature. The laser impinged on the sample via the hole in the top plate of the sample carrier. (b) A schematic view of the system of valves with which the temperature quenches were effected. The high-temperature regulator sensed the thermistor adjacent to the sample cell and in turn drove a heater mounted on the brass block. The solenoid valve was closed during this period and the shunt valve allowed the bath water to continue circulating. For the quench the solenoid was opened, the heater turned off, and the shunt closed. The thermistor was then used to monitor the sample temperature.

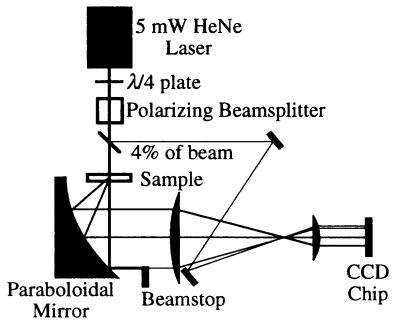

FIG. 3. Plan view of the light-scattering apparatus. The light from the 5-mW HeNe laser impinged on the sample via an attenuator (quarter-wave plate and polarizing beam splitter) and glass plate oriented to extract, from the incident beam, an intensity-calibration beam. The sample sat at the focus of an off-axis paraboloidal mirror capable of collecting light scattered by up to 45° from incidence. The pattern of scattered light, a remnant of the main beam, and the intensity-calibration beam were than transferred to a 14-bit CCD camera connected to a personal computer. The apparatus had two decades of dynamic range in scattered-photon momentum transfer, and nearly five decades in intensity.

to yield the best resolution in the structure function. The fine adjustments of the optical apparatus' design were made with a three-dimensional ray-tracing program.

In order that there was an on-board calibration of the incident intensity, a glass flat was inserted upstream of the sample and oriented to reflect approximately 4% of the incident beam onto secondary flat mirrors which in turn directed it onto a masked portion of the CCD. The spot thus formed was integrated and used to normalize the structure data, thus allowing a direct comparison of intensities, regardless of the upstream attenuation of the incident beam. The beam stop used was simply a highly absorptive neutral density filter. By allowing a remnant of the main beam to pass onto the detector we could locate the position of zero momentum transfer with certainty, as well as check the turbidity of the sample on-line to make sure we were still in the single scattering regime.

The final complexity in the design of the optics was calibration of the mapping from photon momentum transfer to position on the CCD, and verification that all rays which were scattered into a given direction led to a single pixel. In the scattering plane (the page in Fig. 2), this was effected by placing a 100 line pair per millimeter grating in the position of the sample. When the sizes of the interference peaks, where they hit the CCD, were less than one pixel, the requirement that all scattered rays emanating from a plane perpendicular to the incident beam direction, into a given direction, hit the same pixel, was satisfied. In order to extend this result to the rest of the scattering volume, the grating was moved parallel to the incident beam a total of 1 mm. In order to fully calibrate the entire surface of the CCD, a jig was made to rotate the grating in a plane perpendicular to the incident beam. The set of coaxial light cones which resulted from the interference maxima of the grating being swept through 180° were imaged by making an exposure of duration appropriate to the angular velocity of the grating, i.e., half the period of rotation. This step allowed us to confirm that the curves created in this manner were no more than one pixel thick, provided the grating plane was within the scattering volume.

Furthermore, we were able to assess the symmetry of these curves as a confirmation of the correct alignment of the off-axis paraboloidal mirror, and finally we could fully calibrate the entire surface of the CCD.

III. EXPERIMENT: SAMPLE PREPARATION

The atactic *cis*-1,4 PI material, $[C_5H_8]_N$, was synthesized using the anionic polymerization technique with sec-butyl lithium as the initiator. Chains were proton terminated. These samples contained approximately 20% trans configured material and approximately 5% 3,4-PI. These contamination levels were assessed using solution nuclear-magnetic-resonance (NMR) spectroscopy. For the present studies, PI with molecular weight 2000, corresponding to a polymerization index N of 29 ± 1 was used in the blends. The PEP material, $(C_5H_{6.4}D_{3.6})_N$, was made from another batch of PI (with $N=73\pm1$) by saturating the double bonds in a high-pressure deuteration process. The deuteration was catalyzed with palladium on a calcium carbonate support, and resulted in both straight addition and substitution of deuterium. H-D stoichiometry was determined using the density gradient column technique. The polymer was dissolved in cyclohexane in a 2% by weight solution. Deuteration was carried out in a bomb reactor at 70 °C under 34-atm deuterium gas pressure. The polymer solution was stirred under these conditions for 24 h. Bond saturation exceeded 99.5% as determined by solution NMR.

Deuteration, not hydrogenation, was used in the preparation of the PEP in order to match the densities of the blend constituents over the range of temperatures of interest. Density mismatch never exceeded 0.1% in the present experiments, eliminating gravity as a possible effect in the phase-separation dynamics. The molecular weights used were chosen to render the critical temperature in the neighborhood of room temperature. Homogeneous blends were ensured by mixing dilute solutions of the PEP and PI together at temperatures well in excess of the critical temperature and then drying them in a vacuum oven. Samples were then loaded into the cells described above and stored in an oven at 60 °C in preparation for the quench experiments. The glass transition temperature for all samples was below −50 °C.

IV. EXPERIMENT: DATA ACQUISITION AND PROCESSING

A dilution series of samples was prepared with volume fraction PI ranging from 0.32 to 0.84 in increments of 0.04. Each of these samples was then cooled from the storage temperature of 60 °C until a sharp increase in the forward scattering was observed to occur. Provided the cooling rate is sufficiently slow compared to the time for phase-separating domains to reach a size comparable to the wavelength of the laser light, "cloud-point" measurements of this sort yield a reliable estimate of the position of the phase-separation threshold, the locus of which for all concentrations constitutes the coexistence curve. This sort of procedure resulted in Fig. 1. It is notable that the samples never actually became cloudy. In order to stay in the single scattering regime we required the attenuation due to scattering to stay below 20%, even in the late times. Once the phase-coexistence curve was determined by this method for each member of the dilution series, a best fit was made to the data using the Flory-Huggins free-energy density [22],

$$f(\varphi)=\frac{\varphi\ln\varphi}{N_{\rm PI}}+\frac{(1-\varphi)\ln(1-\varphi)}{N_{\rm PEP}}+\chi\varphi(1-\varphi)\ , \qquad (1)$$

where φ is the volume fraction of PI in the mixture, and $N_{\rm PI}$ and $N_{\rm PEP}$ are the polymerization indices of the two species. The Flory interaction parameter has temperature dependence given by

$$\chi(T)=\frac{a}{T}+b\ , \qquad (2)$$

so below T_c, $f(\varphi)$ has the familiar double-well form. Given that the chemical potential μ is equal to $\partial f/\partial\varphi$, it follows that the equilibrium compositions of the coexist-

ing phases will be given by the abscissas of the two points on the free-energy density curve which have a common tangent. It is the locus of these common tangency points which makes up the coexistence curve. The stability of a concentration fluctuation, furthermore, is given by the curvature of the free-energy density, so that the locus of inflection points in $f(\varphi)$ is the stability threshold. Inside this curve, called the spinodal, the homogeneous state is thermodynamically unstable, and the phase separation proceeds via spinodal decomposition, at least in the classical mean-field picture [23]. The classical spinodal is depicted as a dashed line in Fig. 1. Between the spinodal and coexistence curve, the disordered state is metastable, and the phase separation proceeds via nucleation and growth. In this region, infinitesimal amplitude fluctuations dissipate, while those exceeding a critical amplitude and critical size are able to grow. The a and b of (2) are the only parameters of the fit. They are 51.9 K and -0.12, respectively, for the curve shown in Fig. 1. Independent small-angle neutron-scattering measurements [24] of the binary-liquid structure in the one-phase region yielded $a=26.5$ K and $b=-0.037$, which compare favorably with the phase-diagram determination of these parameters. Notice that the critical composition

$$\varphi_c=\frac{\sqrt{N_{\mathrm{PEP}}}}{\sqrt{N_{\mathrm{PEP}}}+\sqrt{N_{\mathrm{PI}}}}\approx 0.6 \tag{3}$$

is not a fitting parameter. The success of the theory to correctly identify ϕ_c is encouraging when relying on the Flory-Huggins theory for binary-polymer mixtures. For those compositions far from criticality, the Flory-Huggins theory appears to have failed to reflect the position of the coexistence curve as determined on the basis of the cloud-point measurements. One must realize that the volume fraction of the minority phase becomes vanishingly small close to the coexistence curve as the composition deviates significantly from critical, as does the signal in the previously described measurement of the onset of strong forward scattering. In actuality, by the time the signal can be measured, the system may have been rather deeply quenched into the metastable region. Far from criticality, cloud-point measurements are not expected to be reliable determinants of the coexistence curve. This is of little consequence for the results being reported here. For the two samples of interest ($\varphi=0.48$ and 0.60), the position of the onset of phase separation was determined to an accuracy of 5 mK.

For both the critical and off-critical quenches, the experiment consisted of allowing the sample to equilibrate in the disordered state, approximately 0.1 °C above the phase-separation threshold, and then effecting a quench to a final temperature below the phase-separation threshold by between approximately 0.1 °C and 1.0 °C. After the quench, determinations of the structure were made by measuring the scattering with the CCD camera, with the interval between measurements typically increasing exponentially, in deference to the power-law behavior observed in the measurable quantities over some time window. At the high temperature equilibration point, the temperature was regulated by the Lakeshore temperature controller. The temperature was read with a Yellow Springs Instruments thermistor with a nominal resistance of 100 kΩ at 25 °C. The controller in turn supplied current to the Minco tape heater attached to the brass block as described in Sec. II. The quench was effected by simultaneously turning off the heater and routing water of preregulated temperature through the passages of the brass block. This was was pumped from a Lauda circulator and regulator, resulting in characteristic quench times on the order of 15 to 20 s. Typical temperature-profile data are shown in Fig. 4 for a variety of quenches.

The structure functions were calculated by averaging together 11 adjacent rows of the CCD, the row corresponding to the scattering plane, and the five rows both above and below this plane. This averaging helped reduce the speckle in the structure functions, and increased the sensitivity to low light levels at large momentum transfer by improving the photon counting statistics. For each quench, at time $t=0$, the scattering function was measured before the phase separation started. These data were subtracted from all subsequent data sets to eliminate the effects of scattering from imperfections on the glass surfaces and any other static effects, such as the dark current from the CCD chip. The transformation from pixel index to photon momentum transfer, q, was effected with the calibration curve which was measured as described in Sec. II above.

With this, the reader will notice that the expectations of the experiment were conceptually rather modest. In the case of the off-critical quench, we merely sought to measure the mean radius and polydispersity, as a function of time, of the distribution of droplets that nucleate and grow after quenching into the metastable region of the phase diagram. Our method allowed us to make very accurate determinations of these dynamical variables in

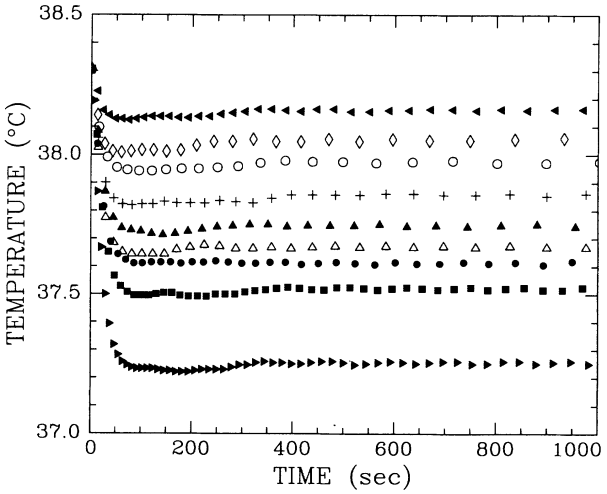

FIG. 4. Traces of temperature vs time for several quenches. Only the first 1000 s are shown, the stability indicated for that period being typical of that observed for quenches of up to 10^6 s duration. The quench time was about 30 s, regardless of quench depth, and except for a transient of approximately 200 s duration, the temperature remained stable to within ±5 mK of the quench temperature.

the range of time for which the polydispersity did not exceed approximately 12%. For the critical quenches, we endeavored to measure the characteristic length scale of the spinodal pattern as it coarsened in time. With the excellent dynamic range of the CCD, we were able to determine the existence of two nonlinear growth modes, each characterized by a different kinetic exponent.

V. EXPERIMENT: RESULTS AND DATA ANALYSIS

A. Monodispersed spheres

For off-critical quenches, we modeled the scattering as essentially that from a dispersion of dielectric spheres, with Gaussian distributed radii of width σ and mean R_0, neglecting coherent (structural) effects between spheres. The distribution of sphere radii is given by

$$n_{\sigma,R_0}(R)=\frac{N}{\sigma\sqrt{2\pi}}\exp\left[\frac{-(R-R_0)^2}{2\sigma^2}\right], \tag{4}$$

where N is the number density of spheres in the scattering volume. The form for the scattering from a single dielectric sphere in the Rayleigh-Gans limit is given by [25]

$$\Sigma_R(q)=\left[\frac{4\pi}{3}R^3 j_1(qR)\right]^2 = \left[\frac{4\pi}{q^3}(\sin qR - qR\cos qR)\right]^2, \tag{5}$$

where j_1 is the first spherical Bessel function. The total scattering signal for such an uncorrelated dispersion of spheres is

$$S_{\sigma,R_0}(q)=\int_0^\infty n_{\sigma,R_0}(R)\Sigma_R(q)dR\ . \tag{6}$$

After a little algebra, and some simplification based on the fact that we expect σ to be significantly smaller than R_0, we get the following function which we used to fit the data:

$$S_{\sigma,R_0}(q)=I_0 u^{-6}\{1+u^2+e^{-2q^2\sigma^2}[(u^2-1)\cos 2u-2u\sin 2u]\}\ , \tag{7}$$

where $u=qR_0$. The parameters of the fit were R_0, σ, and $I_0=N(4\pi R_0^3/3)^2$; all are functions of time. This fitting function was not expected to be valid in the limit $q \ll R_0^{-1}$, where the structure function deviates from the uncorrelated-sphere approximation due to coherent scattering effects. For $q > R_0^{-1}$, $S_\sigma(q)$ is an excellent approximation to the scattering from a dispersion of spheres, and in practice yielded very reliable determinations of σ and R_0 Ref. [26]. Notice that in the limit that $\sigma \to 0$ we recover the single sphere scattering:

$$S_{0,R_0}(q)=\Sigma_{R_0}(q)\ . \tag{8}$$

Figure 5 shows measured structure functions with their best-fitted $S_{\sigma,R_0}(q)$ shown as a solid line, for several typical values of σ and R_0. The small-q deviation between the model function and the data is consistent with suppression of forward scattering due to coherent effects between spheres, in the form of a liquid structure factor. There is the possibility of further attenuation in the near-forward direction due to the form factor for the depletion zone which surrounds each droplet. We have not attempted to model these effects in our fit functions.

In order to put an upper limit on the polydispersity, σ, we allowed the higher-q data more weight in the fits. This was effected by assigning a weight factor for the ith data point in the structure factor $w_i=S_i^{-1}$, where S_i is the intensity for that point. We wanted to ensure that the polydispersity parameter was well determined. This means that by counting the number of resonances which are discernible in the structure function, one may determine the ratio $\mu=\sigma/R_0$ directly. The model function tended to overestimate the depths of the low-q nodes when the recipe outlined above for the determination of μ was followed, though this can barely be seen in Fig. 5. This failure on the part of the modeling has been attributed to weak multiple-scattering effects. Multiple scattering of about 10% of the photons would easily account for the shallow nodes (being in mind that the intensity axis in Fig. 5 has a logarithmic scale), without affecting the determination of σ and R_0.

Figure 6(a) shows the evolution of the radius of the spheres plotted as a function of time on logarithmic axes. A line with slope $\frac{1}{2}$ is also plotted, to demonstrate that with minimal deviation, we observed the growth law

$$R(t)\sim t^{1/2} \tag{9}$$

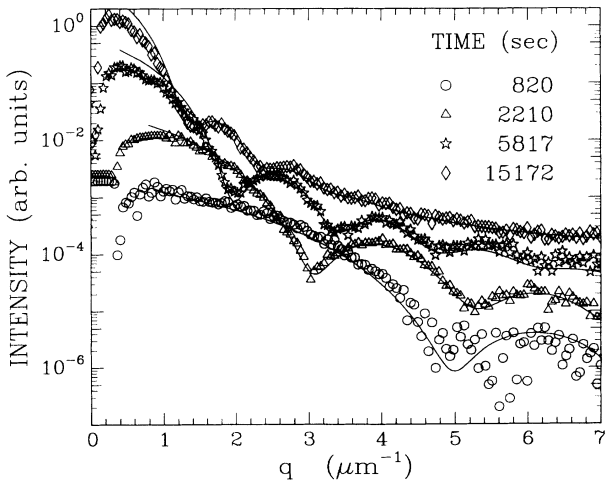

FIG. 5. Monodisperse-spheres structure functions for several times as indicated after a quench of $\Delta T=0.40$ °C into the coexistence region at $\varphi_{PI}=0.48$. The mean radii as fitted by (7) in the text are 0.868, 1.46, 2.28, and 3.31 μm for the earliest to latest times, respectively. The polydispersity parameters, σ/R_0, for the same times are 7.4%, 7.9%, 7.5%, and 11.1%.

over the range of time that the polydispersity is small enough to allow fitting by the model function of (7). Figure 6(b) shows the radius-normalized polydispersity, μ, as a function of time for the $\Delta T=0.40\,^{\circ}\mathrm{C}$ quench whose radii appear in Fig. 6(a). One can see that over the range of times for which the polydispersity is measurable, there is a distinct tendency towards a minimum, followed by an increase. The final piece of experimental certainty is evident in Fig. 7, wherein we have plotted the intensity prefactor of the fits, I_0, versus the radius, R_0, on logarithmic axes. From (7) we expect

$$I_0=N\left[\frac{4\pi R_0^3}{3}\right]^2, \tag{10}$$

so the fact that we observed $I_0\sim R_0^6$, as shown in Fig. 7, is quite convincing evidence that over the range for

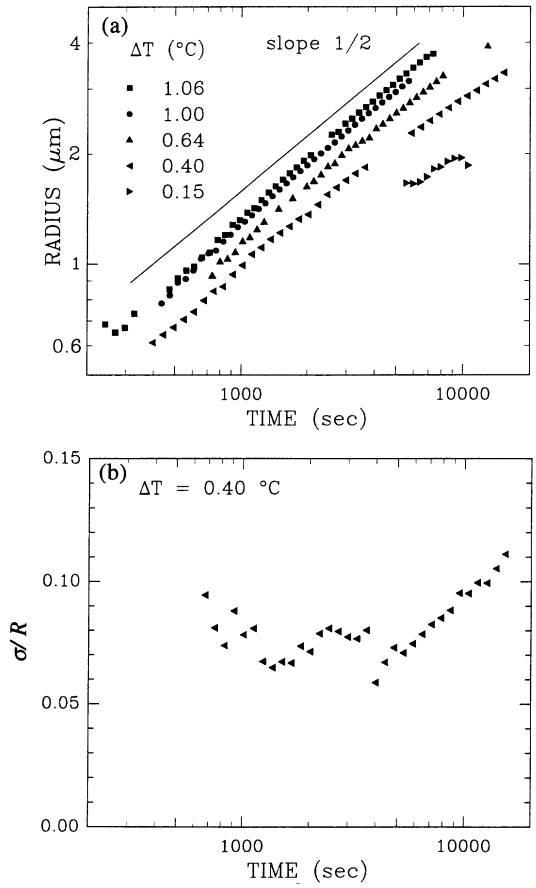

FIG. 6. Radius and polydispersity vs time for the monodisperse spheres. (a) R_0 as fitted by (7) for various quench depths. Notice that for the shallowest quench ($\Delta T=0.15\,^{\circ}\mathrm{C}$), there was only a small time window for which the polydispersity was sufficiently small to allow fitting by (7). A line with slope $\frac{1}{2}$ has been plotted for comparison, to show that $R\sim t^{1/2}$ is approximately obeyed throughout the monodisperse regime. (b) Polydispersity σ/R_0 for the 0.40 °C quench, showing a high value (about 10%) at early times, then decreasing to a minimum (about 6% in this case), and then rising again as the droplets began to interact. In deeper quenches we observed polydispersities as low as 3%.

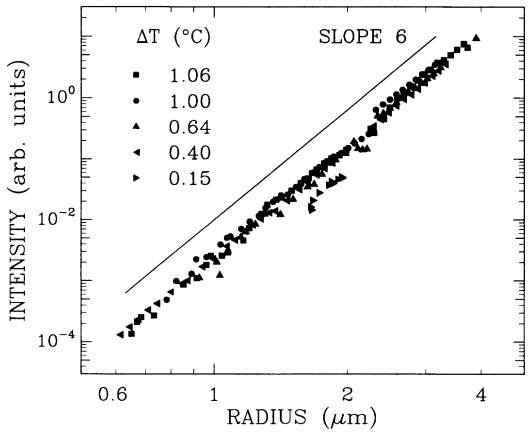

FIG. 7. The best indication that the number density of spheres remained constant during the monodisperse regime. The intensity prefactor I_0 of fits to (7) plotted vs mean radius R_0 for those fits, clearly showing the $I_0\sim R_0^6$ relationship discussed in the text.

which we were making the measurements, the total number of spheres in the scattering volume, N, remained constant. Furthermore, to compare the values of N for different quenches, we fit the I_0 versus R_0 data with the the function $f(x)=bx^6$. The prefactor b from these fits is proportional to N, and except for some scatter which is to be expected in such heavily processed data, not only is N constant in time for a given quench, it would appear to be almost constant from quench to quench at distinct temperature differences. This fact is reflected in the strong clustering of the data at different quench depths along the same slope-6 line in Fig. 7.

While the droplet-radius distribution is narrow, Eq. (7) is an excellent model function for the determination of the average radius. As was noted above, however, R_0 cannot be reliably determined once the scattering resonances at higher q values have been washed out. In this regime, we resorted to fitting the Porod [27] slope to the tail of the structure function. Clearly in the short-length limit, the scattering is determined by the details of the interface between the two phases. In three dimensions, and for sharp interfaces, the tail is expected to have the following functional form:

$$\lim_{q\to\infty} S(q)=Pq^{-4}. \tag{11}$$

The Porod slope, then, is -4, by virtue of the fact that when S versus q is plotted on logarithmic axes, it tends to a straight line with slope -4 as q gets large. This is shown in Fig. 8 for the tails of several structure functions measured at various times after a quench of 0.31 °C into the two-phase region at $\varphi_{\mathrm{PI}}=0.44$. The prefactor P of a Porod-law fit is proportional to the total interfacial area in the scattering volume [28], and is shown as a function of time for this quench in Fig. 9. During the free-growth regime, when the droplets do not interact, their mean radius can be seen in Fig. 6(a) to grow as $t^{1/2}$, which, since their number remains constant, means that the surface

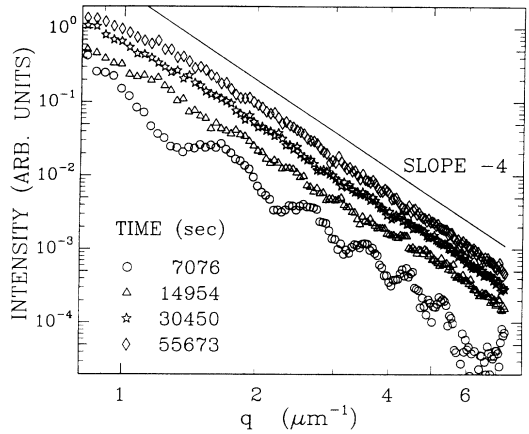

FIG. 8. Porod-law fits to the high-q portion of the structure functions. The intensity has undergone a background subtraction. The Porod prefactor [see Eq. (11)] is proportional to the total surface area within the scattering volume. For earlier times, when the structure function was ringing due to the monodisperse distribution of droplet radii, this parameter was not as well determined as it was at later times. The Porod slope of -4 is shown for direct comparison with these structure functions.

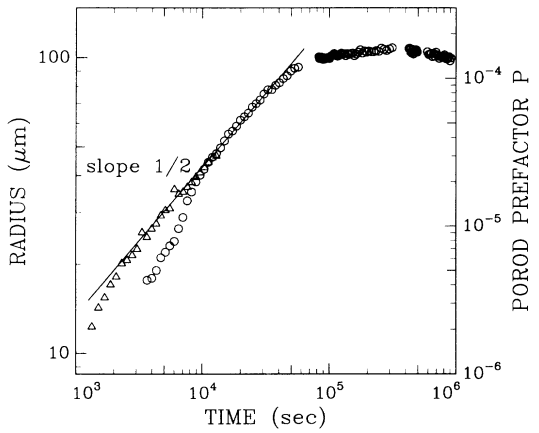

FIG. 9. The Porod prefactor vs time for an off-critical quench of $\Delta T=0.31\,^{\circ}\mathrm{C}$. The circles indicate the time-evolution of the prefactor in fits of the sort illustrated in Fig. 8. This prefactor is proportional to the interfacial area of the scattering structure, as discussed in the text. In the free-growth regime we observed $R_0 \sim t^{1/2}$, so $P \sim t$, as expected. The triangles are droplet radii as determined by fits to (7), and the line has slope $\frac{1}{2}$ on the radius (left) axis) and slope 1 on the prefactor (right) axis. The two techniques are complementary in that when (7) is a good model for the structure function, the Porod prefactor is poorly determined due to the high-q ringing, as indicated by the deviation of the circles from power-law behavior at earlier times. It is interesting to note that in the limit of fully-interacting droplets, when the volume of minority phase had saturated at its equilibrium value, we expected the radius to behave as $t^{1/3}$. In this Lifshitz-Slyozov coarsening regime, we therefore expected the Porod prefactor to cross over to a $t^{-1/3}$ behavior, as was indeed observed as the time approached 10^6 s.

area grows as t. This is reflected in the slope of 1 (as read from the right-hand scale; $\frac{1}{2}$ is for the left-hand scale) in the earlier stages of the plot in Fig. 9. After approximately 10^5 s, there has been a crossover to the fully-interacting-droplet regime, where the volume fraction of minority phase has saturated at its equilibrium value, and thereafter remains constant. In this regime, mean droplets radius is expected on the basis of Lifshitz-Slyozov theory to increase as $t^{1/3}$, meaning that the total interfacial area, hence P, should behave like $t^{-1/3}$. This is indicated by the crossover to a slope of $-\frac{1}{3}$ at about 5×10^5 s in Fig. 9.

B. Fast mode

For the critical quenches, we observed the well-known ring associated with the bicontinuous infinite-cluster morphology seen in spinodal decomposition [29]. There is an extensive literature concerning appropriate choices for the line shape appropriate to this sort of structure function [30]. Figure 10 shows the temporal evolution of the structure function after a quench of a sample at the critical composition $\varphi_c=0.60$ by $0.64\,^{\circ}\mathrm{C}$. The two modes, that corresponding to the standard growth exponent of $\frac{1}{3}$, and the fast mode with its attendant $\frac{3}{2}$ growth, can clearly be seen to develop as time evolves. Figure 11 is a photomicrograph of the sample during phase-separation again clearly showing the large-sale structure of the fast mode and the smaller-scale structure of the slow mode. In the present research we were most interested in finding the time evolution of the peak position, and so chose a simple form for the model line shape:

$$S(q)=\frac{I_0(t)}{\{1+x^2[q-q_m(t)]^2\}^2}\ . \tag{12}$$

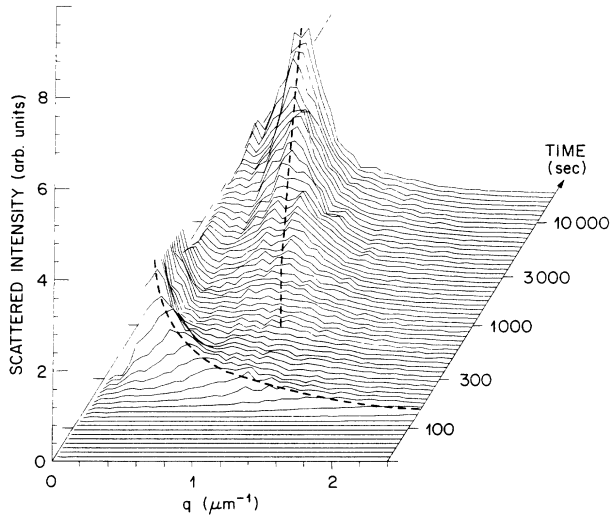

FIG. 10. The scattered intensity as a function of photon momentum transfer q at various times after a $0.65\,^{\circ}\mathrm{C}$ quench below the critical temperature T_c. The loci of the maxima of the fast-mode peak and the slow-mode peak are indicated by dashed lines. The maximum intensities for the two peaks displayed are 3.4 and 2.0 arb units for the slow and fast modes, respectively.

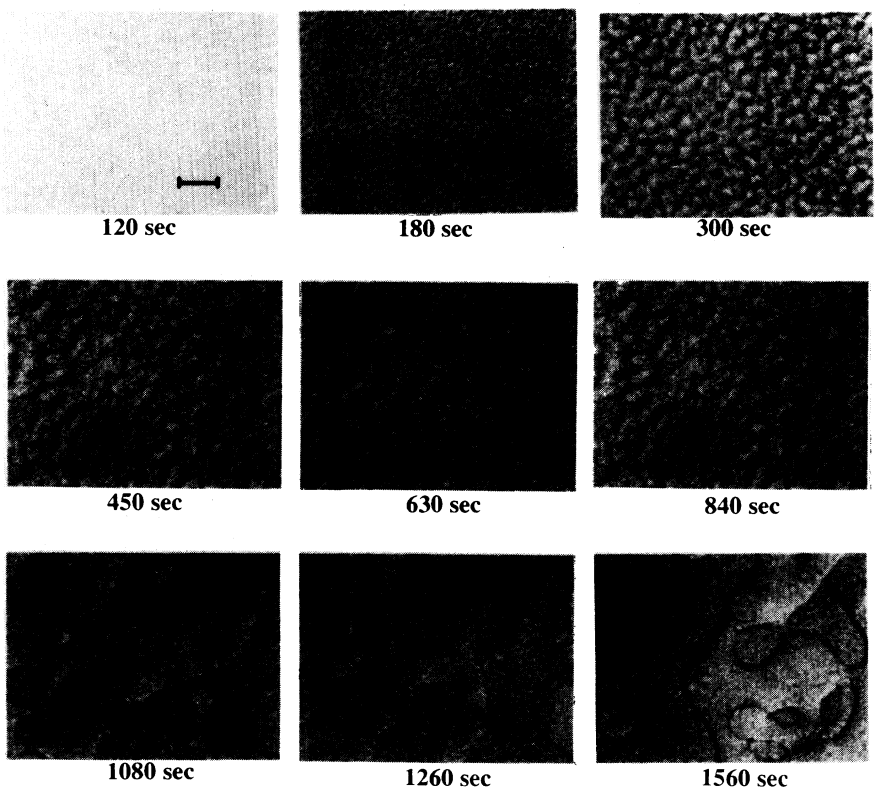

FIG. 11. A series of photomicrographs of the fast-coarsening structure. At times greater than 400 s the coexistence of the two different length scales corresponding to interface and bulk growth is visible. The magnification in all the pictures is the same and the length of the bar in the first picture is 50 μm.

This model function was chosen simply because it has the necessary features of a quadratic maximum for the peak, and in the large-q limit, $S(q) \sim q^{-4}$, in accordance with the Porod law for scattering from an interface. We were primarily interested in the peak position as a function of time, $q_m(t)$, and the maximum scattered intensity as a function of time, $I_0(t)$, so this function served very well as a peak finder when fitted to the data with a nonlinear least-squares fitting routine. We limited the range of the fitting in q space to approximately the interval $q_m \pm q_{h/2}$, where $q_{h/2}$ is the difference between q_m and the point where the structure function falls to half its peak value. The parameter x, with dimensions of length, reflects the full width at half maximum, i.e., $\Delta q = 1.29/x$. Figure 12 shows typical structure functions at various times after a quench of $\Delta T = 0.25\,^{\circ}\mathrm{C}$ below the critical temperature. Also indicated is the interval for peak fitting to (13) and the model line shape on that interval. Clearly in the region of interest the model function adequately mimics the data, so that the fitting parameters I_0 and q_m could be determined as a function of time. For those structure functions with both a fast-mode and a slow-mode peak evident, initial values of the parameters had to be inserted by hand into the nonlinear least-squares fitting routine for each of the two peaks separately, so that both peaks could be found. Figure 13 shows typical plots of the peak in the structure function, q_m, versus time, t, on logarithmic axes, showing the fast and slow modes' coarsening behavior as a function of quench depth.

There have been numerous experiments performed [31,32] which confirm the hypothesis of dynamical scaling [33,34] in phase-separating fluids. Asymptotically, the morphology of the phase-separating domains is expected to approach a form which is self-similar in time. Under these conditions, the structure function is expected to approach a scaling form, wherein all time dependence is carried in a single length scale, $L(t) \sim [q_m(t)]^{-1}$, as follows:

$$S(q,t) = [q_m(t)]^{-d} F\left[\frac{q}{q_m(t)}\right], \tag{13}$$

where d is the dimensionality of the scattering structure. Notice that there is no explicit time dependence in the scaling function F, and so the intensity prefactor of the fitted structure function should scale with peak position, i.e., $I_0(t) \sim [q_m(t)]^{-d}$. We sought to confirm that the slow mode was associated with coarsening of a three-dimensional structure by plotting I_0 versus q_m^{-1} on logarithmic axes and showing that the locus of such points fell on a line with a slope of three corresponding to $d = 3$. We made similar plots for the fast-mode data and found that they again fell on a line, but with slope two, suggesting that the fast-mode structure is two dimensional. Fig-

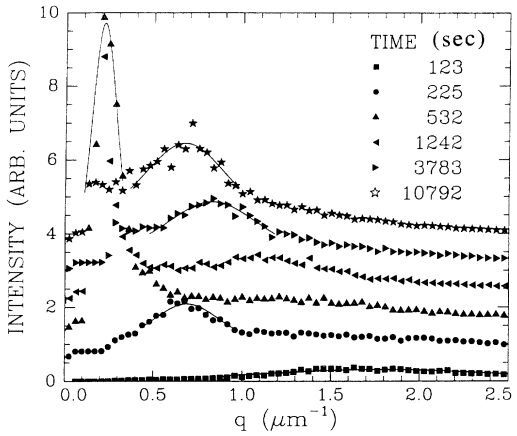

FIG. 12. Structure functions at various times after a quench of 0.25 °C below T_c. The first three, at 123, 225, and 532 s, show the fast-mode peak at approximately 1.8, 0.7, and 0.2 μm^{-1}, respectively. In the next one, at 1242 s, the fast mode has gone forward into the beam stop, but the slow mode is just beginning to emerge at 1.1 μm^{-1}. The final two structure functions show the slow-mode peak at about 0.9 and 0.7 μm^{-1}. Fits to (12) over the q range discussed in the text are illustrated for several data sets. Each successive structure function has had 0.8 arb.units added to give the figure greater clarity.

ure 14 shows data for the 0.15 °C quench. Further investigation with the microscope indicated that the structure associated with the fast-mode growth was confined to an approximately 10-μm-thick layer adjacent to the quartz windows which contain the sample. Obviously, if dynamic scaling were to apply strictly for both the bulk and the surface, the two subsystems could not be in diffusive contact with each other. We plotted S/I_0 versus q/q_m to confirm that dynamical scaling approximately applied over the range of times measured. At very late times,

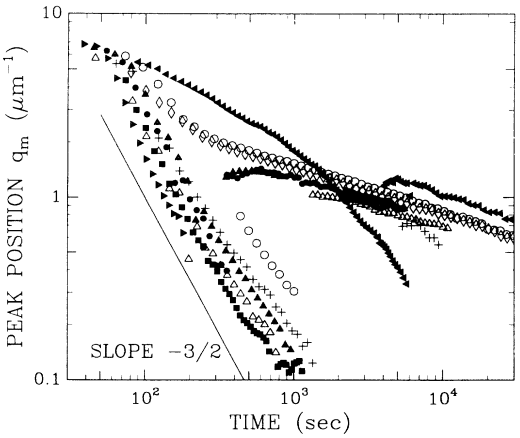

FIG. 13. Peak position in q space vs time for ten different quenches ranging in depth from 0.15 °C and 1.00 °C, represented by the left-pointing triangles and right pointing triangles, respectively. The shallowest two showed simultaneous fast-mode and slow-mode behavior, as indicated in the figure. Several others showed both modes, though not at the same time. The deeper quenches showed only the fast mode, presumably because the fast mode filled the entire sample cell before the slow (bulk) effect had the opportunity to manifest itself.

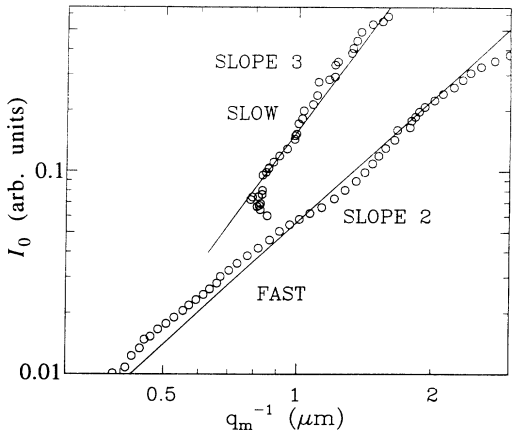

FIG. 14. Peak intensity of the fast and the slow modes as a function of inverse peak position. The slopes of these lines give the dimensionality of the scattering structure, under the assumption that dynamical scaling holds for both processes.

however, the surface and bulk subsystems must come into some sort of quasiequilibrium, because eventually the surface pattern disappears completely, presumably as a complete wetting layer of the preferred phase forms, as was suggested in the seminal work of Cahn [35] on the subject of wetting in phase-separating systems.

VI. DISCUSSION

A. Monodispersed spheres

An isolated droplet of one phase, in diffusive contact with a supersaturated sea of another phase, will grow, provided the energy released by reducing the supersaturation condition in that region of space is more than the energy required to construct the interface which encloses the sphere. Since the former of these quantities scales as R^3, where R is the radius of the sphere, and the latter as R^2, the sphere is viable and will grow provided it is large enough. By solving the diffusion equation with the appropriate spherical boundary condition, and with the incorporation of these ideas, a rate equation for the radius of such a sphere can be deduced [36,14]:

$$\frac{dR}{dt} = \frac{D}{R}\left[\Delta - \frac{\alpha}{R}\right] . \tag{14}$$

D is the diffusion coefficient, Δ is the relative supersaturation, and α is the interface thickness. Δ is expressed in terms of the equilibrium compositions of the coexisting minority (droplets) and majority phases, and the overall composition of the sample, φ_0, by

$$\Delta = \frac{\varphi_{\text{maj}} - \varphi_0}{\varphi_{\text{maj}} - \varphi_{\text{min}}} . \tag{15}$$

For $R > \alpha/\Delta$ in (14), dR/dt is positive and the sphere grows. $R^* = \alpha/\Delta$ is the critical radius for the viability of a droplet. Using the ideas of Binder [37] we can construct a formula for the critical radius as a function of the temperature of the quench and the supersaturation,

$$R^* = \frac{a}{4}\sqrt{N}\left[\frac{T_c - T}{T_c}\right]^{-1/2}\Delta^{-1} . \quad (16)$$

Here, a is some statistical segment length for the monomer unit, taken as 5 Å for the current work. N was taken to be 40 for the purposes of this calculation. A similar formula for R^* can be derived from the ideas presented in the work of Joanny and Leibler [38] on interface profiles in polymer melts, except the numerical prefactor is $\frac{1}{3}$ instead of $\frac{1}{4}$. We offer no explanation for this discrepancy, but used the Binder version simply because it is the more recent. For the off-critical sample used here, the temperature at the phase-separation threshold was 1.63 °C below the critical temperature. This was taken into account when calculating R^* from (16) by using $T_c - T = 1.63\,°C + \Delta T$, where ΔT is the actual quench depth below the coexistence curve. There is variable rescaling suggested by (14), in that if we rescale the radius by the critical radius, defining dimensionless radius

$$\rho = \frac{R}{R^*} = \frac{R\Delta}{\alpha} , \quad (17)$$

and likewise create a dimensionless time τ in the following way,

$$\tau = \frac{D}{\alpha^2}\Delta^3 t , \quad (18)$$

we can rewrite (14) as follows:

$$\frac{d\rho}{d\tau} = \frac{1}{\rho}\left[1 - \frac{1}{\rho}\right] . \quad (19)$$

The diffusion constant D has been measured by dynamical light scattering [24] to be 9.0×10^{-11} cm^2/s, so that all quantities needed to effect the variable rescaling of (17) and (18) are readily available, either by direct measurement or through (15) and (16). Table I lists these quantities for the R versus t data shown in Fig. 6(a), which were then transformed into ρ versus τ and plotted in Fig. 15. Notice that under the quench-depth-dependent rescaling all the growth data essentially collapse onto a universal curve, with some deviations which we now discuss.

The solid lines in Fig. 15 represent forward integrations of (19) from an early initial time and a variety of initial sizes (all $\rho \geq 1$, the critical reduced radius). As mentioned earlier, this equation models growth of an isolated sphere in an infinite sea of supersaturated phase, which is reflected by a constant Δ. As such, the model functions

TABLE I. Quantities for the scaled ρ vs τ data shown in Fig. 15.

ΔT (°C)	Δ	α (Å)	R^* (μm)
1.06	0.107	18	0.170
1.00	0.102	19	0.184
0.64	0.073	20	0.276
0.40	0.050	21	0.430
0.15	0.021	23	1.10

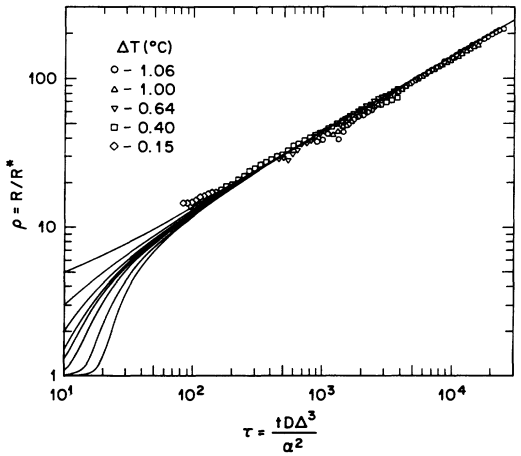

FIG. 15. Plot of the data in Fig. 6(a) with the time axis rescaled by $\alpha^2/D\Delta^3$ and the radius axis rescaled by R^*. The model curves are numerically integrated solutions of (19) for various initial conditions, showing that the monodispersity is a natural consequence of the free growth of nucleated droplets once the nucleation has stopped.

clearly show why the radius distribution can be initially broad, and then, provided no new nuclei are introduced after some critical time, narrows in time to almost an ideal δ function. Indeed, this is what was observed. For all quenches there was a light-scattering signal at times earlier than those for which the radius could be determined, but this distribution in radii was too broad to make effective use of (7) as a fitting function. Another noticeable deviation from the model in Fig. 15 is the tendency of some of the curves, especially those corresponding to the shallower quenches, to roll off at later times. This effect is due to the interaction of the depletion zones which surround each sphere, in the real sample. At some time, depending on the quench depth, the depletion zones begin to interfere with each other, reducing the effective supersaturation, Δ, thereby slowing down the growth of the spheres. As Δ decreases, R^* increases (α being a system-dependent parameter only) until it exceeds the radius of the smaller spheres in the distribution. At some point a dynamical equilibrium obtains wherein all moments of the distribution and R^* grow at the same $t^{1/3}$ rate. This is the LS coarsening regime for a system with a conserved order parameter. Although the mean radius could no longer be measured directly via (7), the Porod-law prefactors plotted in Fig. 9 show the crossover from free growth of isolated spheres to LS coarsening.

We have modified (14) to allow for $\Delta = \Delta(t)$, a dynamical variable. In our integrations, we have required that Δ be coupled to the density of nuclei in the sample, through the insistence that the total mass of each species be conserved. As the droplets grow, and their depletion zones interact, Δ is reduced in accordance with the conservation of mass. We have included sample calculations of this kind in Fig. 16 for deep and shallow quenches, with parameter values similar to those measured. Clearly for the shallow quenches the duration of approximately un-

fettered $t^{1/2}$ growth is shorter than for the deeper quenches, which is consistent with what has been observed in the experiments. We feel that a mechanism of this sort fully explains the deviation of the experimental data from the $t^{1/2}$ growth law at later times in Fig. 15.

B. Fast mode

We do not have a theoretical description of any phenomenon which would account for the observed $t^{3/2}$ growth [39]. By tacitly making the dynamical-scaling assumption, we have observed that the data are consistent with a two-dimensional structure for the fast mode and a three-dimensional structure for the slow mode. This is sensible and satisfying, because we certainly want to know that we can see the conventional diffusion-limited-growth exponent of $\frac{1}{3}$ for coarsening in the bulk. Furthermore, photomicrography studies of the domain morphology in the late stages (after the spinodal rings have collapsed into the beam stop of the scattering apparatus) indicate that the fast mode with its much longer length scales is associated with the surfaces of the sample container. These two facts would indicate that over the complete range of times for which the fast mode is observable, it is somehow related to the surfaces.

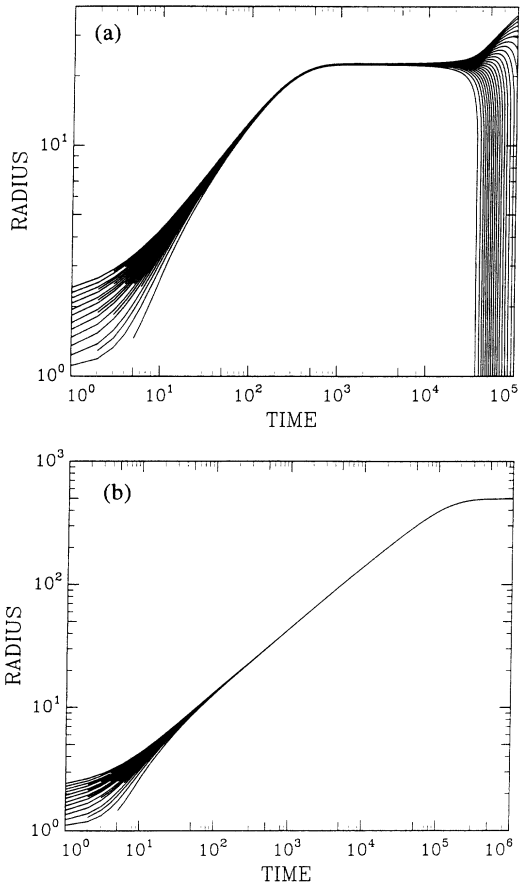

FIG. 16. Model curves obtained by numerical integration of (14) in its dimensionless form. The supersaturation Δ was not held constant, as in Fig. 15, but was a function of time as described in the text. We observe three different regimes. At early times we start the integration with spheres of reduced radius between 1 and 2.5 being created at reduced times times between 1 and 10. During the free-growth period (Δ constant), the distribution sharpens and the radii grow like $t^{1/2}$. As the depletion zones of the spheres overlap the second regime is entered and the growth essentially stops. In the third regime, the smaller droplets evaporate, and the mean radius grows like $t^{1/3}$ [only apparent in (a)]. The initial supersaturation, $\Delta(t=0)$, for (b) is ten times larger than for (a).

We were able to eliminate all gravity-induced instabilities as responsible for the fast mode. Identical experiments under a representative range of conditions were performed with the sample cell oriented with its glass windows both parallel and perpendicular to the gravitational field. The results did mot depend on the orientation qualitatively or quantitatively. Thermocapillarity, or the motion induced by the temperature dependence of the surface tension between the two phases, was also discarded as a possible explanation for the fast-mode dynamics. An estimate can be made of the maximum velocity possible for fluid parallel to an interface, due to a thermal gradient and its attendant gradient in surface tension [40].

$$v_{\max}=\frac{1}{4\eta}\frac{\partial\sigma}{\partial T}h\frac{dT}{dx}\ . \tag{20}$$

Here η is the viscosity (about 300 cp), σ is the interfacial tension between the coexisting phases, h is the approximate maximum domain thickness, taken to be 100 μm for the purposes of this calculation and the thermal gradient, dT/dx, parallel to the glass, was assumed to have a maximum value of 0.1 °C/cm. As there was no radial gradient in the turbidity for shallow quenches, we determined an upper limit on the temperature gradient to be the size of the temperature jump for these smallest quenches. A maximal estimate for $\partial\sigma/\partial T$ can be made by differentiating (18) from Ref. [38]:

$$\frac{\partial\sigma}{\partial T}\approx\frac{k_BT}{\sqrt{N}a^2T_c}\left[\frac{T_c-T}{T_c}\right]^{1/2}\ , \tag{21}$$

where the equality holds in the limit $\Delta T\ll 1$, and a, N, T, and k_B are the monomer length, polymerization index, temperature, and Boltzmann's constant, respectively. Using our deepest quench as an estimate for $T-T_c$, we find that $d\sigma/dT\leq 5\times10^{-4}$, meaning that $v_{\max}\leq 5\times10^{-8}$ cm/sec=0.05 μm/100 s, which is several orders of magnitude smaller than any interface velocities we observe.

By eliminating certain processes as responsible for the fast-mode growth, and observing that the fast-mode growth was associated with the sample windows, we have deduced that there was a preference for the surface on the part of one of the constituent species, that is, there was a wetting effect responsible for this novel and extremely fast growth.

ACKNOWLEDGMENTS

We acknowledge useful interactions with D. Huse, J. Langer, J. Marko, C. Roland, W. van Saarloos, E. Siggia,

and B. Shraiman. A. C. acknowledges support from the NSF through PYI Grant No. DMR-9157031 and from the Division of Sponsored Research at the University of Florida. F. S. B. acknowledges support from the NSF through PYI Grant No. DMR-8957386 and through the Center for Interfacial Engineering, an NSF supported Engineering Research Center at the University of Minnesota.

[1] J. D. Gunton, M. San Miguel, and P. S. Sahni, in *Phase Transitions and Critical Phenomena,* edited by C. Domb and J. L. Lebowitz (Academic, New York, 1983), Vol. 8.
[2] *Dynamics of Ordering Processes in Condensed Matter,* edited by S. Komura and H. Furukawa (Plenum, New York, 1988).
[3] G. M. Thurston *et al.,* in *Physics of Complex and Supermolecular Fluids,* edited by S. A. Safran and N. A. Clark (Wiley-Interscience, New York, 1987).
[4] S. Hashisu and S. Yoshimura, Nature (London) **283**, 188 (1980).
[5] K. Hono and K. I. Hirano, Phase Transitions **10**, 223 (1987).
[6] M. Tomozawa, R. K. MacCrone, and H. Herman, Phys. Chem. Glasses **11**, 136 (1970).
[7] T. Hashimoto, Phase Transitions **12**, 47 (1988).
[8] F. S. Bates and P. Wiltzius, J. Chem. Phys. **91**, 3258 (1989).
[9] W. I. Goldburg, in *Light Scattering Near Phase Transitions,* edited by H. Z. Cummins and A. P. Levanyuk (North-Holland, Amsterdam, 1983).
[10] N. C. Wong and C. M. Knobler, J. Chem. Phys. **69**, 725 (1978); **85**, 1972 (1981); Phys. Rev. A **24**, 3205 (1981).
[11] Y. C. Chou and W. I. Goldburg, Phys. Rev. A **20**, 2105 (1979); **23**, 858 (1981).
[12] T. Kyu and D.-S. Lim, J. Chem. Phys. **92**, 3951 (1990).
[13] P. E. Tomlins and J. S. Higgins, J. Chem. Phys. **90**, 6691 (1990).
[14] I. M. Lifshitz and V. V. Slyozov, J. Phys. Chem. Solids **19**, 35 (1961).
[15] E. D. Siebert and C. M. Knobler, Phys. Rev. Lett. **52**, 1133 (1984); **54**, 819 (1985).
[16] J. Langer and A. J. Schwartz, Phys. Rev. A **21**, 948 (1980).
[17] D. Huse, Phys. Rev. B **34**, 7845 (1986).
[18] H. L. Snyder and P. Meakin, J. Chem. Phys. **79**, 5588 (1983).
[19] P. Guenoun, D. Beysens, and M. Robert, Phys. Rev. Lett. **65**, 2406 (1990).
[20] C. Redon, F. Brochard-Wyart, and F. Rondelez, Phys. Rev. Lett. **66**, 715 (1991).
[21] Z. Chen, J. Noolandi, and D. Izzo, Phys. Rev. Lett. **66**, 727 (1991).
[22] P. Flory, *Principles of Polymer Chemistry* (Cornell, Ithaca, 1953).
[23] J. W. Cahn and J. E. Hilliard, J. Chem. Phys. **28**, 258 (1958).
[24] F. S. Bates. J. H. Rosedale, P. Stepanek, T. P. Lodge, P. Wiltzius, G. H. Fredrickson, and R. P. Hjelm, Phys. Rev. Lett. **65**, 1893 (1990); F. S. Bates *et al.,* J. Chem. Phys. (to be published).
[25] H. C. van de Hulst, *Light Scattering by Small Particles* (Dover, New York, 1981), Chap. 7.
[26] A. Cumming and P. Wiltzius, Phys. Rev. Lett. **65**, 863 (1990).
[27] G. Porod, Kolloid-Z. **124**, 83 (1951).
[28] J. Teixeira, in *On Growth and Form,* edited by H. E. Stanley and N. Ostrowski (Nijhof, Boston, 1986).
[29] S. Komura, Phase Transitions **12**, 3 (1988).
[30] A. Chakrabarti, R. Toral, J. D. Gunton, and M. Muthukumar, J. Chem. Phys. **92**, 6899 (1990).
[31] B. D. Gaulin, S. Spooner, and Y. Morii, Phys. Rev. Lett. **59**, 668 (1987).
[32] T. Izumitani, M. Takenaka, and T. Hashimoto, J. Chem. Phys. **92**, 3213 (1990).
[33] K. Binder and D. Stauffer, Phys. Rev. Lett. **33**, 1006 (1974).
[34] H. Furukawa, Physica **123A**, 497 (1984).
[35] J. W. Cahn, J. Chem. Phys. **66**, 3667 (1977).
[36] E. Siggia, Phys. Rev. A **20**, 595 (1979).
[37] K. Binder, J. Chem. Phys. **79**, 6387 (1983).
[38] J. F. Joanny and L. Leibler, J. Phys. (Paris) **39**, 951 (1978).
[39] P. Wiltzius and A. Cumming, Phys. Rev. Lett. **66**, 3000 (1991).
[40] V. G. Levich, *Physiochemical Hydrodynamics* (Prentice-Hall, Englewood Cliffs, NJ, 1962), p. 388.

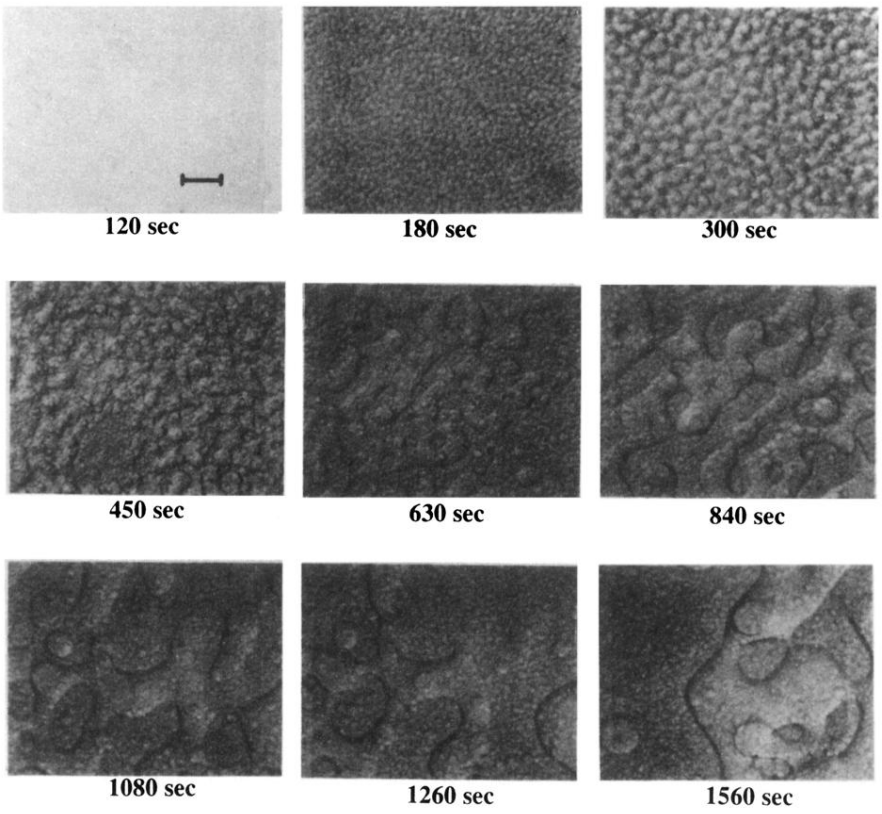

FIG. 11. A series of photomicrographs of the fast-coarsening structure. At times greater than 400 s the coexistence of the two different length scales corresponding to interface and bulk growth is visible. The magnification in all the pictures is the same and the length of the bar in the first picture is 50 μm.